

Wave-like Tunneling of Phonons Dominates Glass-like Thermal Transport in Quasi-1D Copper Halide CsCu₂I₃

Jiongzhi Zheng¹, Changpeng Lin^{2,3}, Chongjia Lin⁴, Baoling Huang^{4,5,6,*}, Ruiqiang Guo^{7,†}, Geoffroy Hautier^{1,‡}

¹*Thayer School of Engineering, Dartmouth College, Hanover, New Hampshire, 03755, USA*

²*Theory and Simulation of Materials (THEOS), École Polytechnique Fédérale de Lausanne, CH-1015 Lausanne, Switzerland*

³*National Centre for Computational Design and Discovery of Novel Materials (MARVEL), École Polytechnique Fédérale de Lausanne, CH-1015 Lausanne, Switzerland*

⁴*Department of Mechanical and Aerospace Engineering, The Hong Kong University of Science and Technology, Clear Water Bay, Kowloon, Hong Kong*

⁵*HKUST Foshan Research Institute for Smart Manufacturing, Hong Kong University of Science and Technology, Clear Water Bay, Kowloon, Hong Kong, China*

⁶*HKUST Shenzhen-Hong Kong Collaborative Innovation Research Institute, Futian, Shenzhen 518055, China*

⁷*Thermal Science Research Center, Shandong Institute of Advanced Technology, Jinan, Shandong Province, 250103, China*

Abstract

Fundamental understanding of thermal transport in compounds with ultra-low thermal conductivity remains challenging, primarily due to the limitations of conventional lattice dynamics and heat transport models. In this study, we investigate the thermal transport in quasi-one-dimensional (1D) copper halide CsCu₂I₃ by employing a combination of first principles-based self-consistent phonon calculations and a dual-channel thermal transport model. Our results show that the 0-K unstable soft modes, primarily dominated by Cs and I atoms in CsCu₂I₃, can be anharmonically stabilized at ~ 75 K. Furthermore, we predict an ultra-low thermal conductivity of $0.362 \text{ Wm}^{-1}\text{K}^{-1}$ along the chain axis and $0.201 \text{ Wm}^{-1}\text{K}^{-1}$ along cross chain direction in CsCu₂I₃ at 300 K. Importantly, we find that an unexpected anomalous trend of increasing cross-chain thermal conductivity with increasing temperature for CsCu₂I₃, following a temperature dependence of $\sim T^{0.106}$, which is atypical for a single crystal and classified as an abnormal glass-like behavior. The peculiar temperature-dependent behavior of thermal conductivity is elucidated by the dominant wave-like tunnelling of phonons in thermal transport of CsCu₂I₃ along cross-chain direction. In contrast, particle-like phonon propagation primarily contributes to the chain-axis thermal conductivity across the entire temperature range of 300-700 K. The sharp difference in the dominant thermal transport channels between the two crystallographic directions can be attributed to the unique chain-like quasi-1D structure of CsCu₂I₃. Our study not only illustrates the microscopic mechanisms of thermal transport in CsCu₂I₃ but also paves the way for searching for and designing materials with ultra-low thermal conductivity.

Keywords: Particle-like phonon propagation, Wave-like tunnelling of phonons, Cubic and quartic anharmonicities, Anharmonic phonon renormalization, Lattice thermal conductivity, Metal Halides.

* mebhuang@ust.hk

† ruiqiang.guo@iat.cn

‡ Geoffroy.t.f.hautier@dartmouth.edu

I. INTRODUCTION

The effective management and utilization of thermal energy are vital for enhancing the operational efficiency and prolonging the lifetime of thermal data storage devices [1], photovoltaic [2-5] and optoelectronic devices [6], along with thermoelectric systems [7-9]. Halide perovskites have shown attractive prospects for photovoltaics and optoelectronics due to their outstanding properties, including a tunable band gap, high absorption coefficients, large carrier mobilities, long diffusion lengths, and exceptional defect tolerance [10,11]. Heat dissipation via phonon thermal transport and the lattice dynamics have a significant impact on the thermal stability, carrier lifetime, and optoelectronic performance of crystalline halide perovskites [12-14]. Furthermore, halide perovskites have recently gained interest in thermoelectrics for thermal-to-electric energy conversion, thanks to their advantageous electrical properties [15-17] and minimal thermal conductivity [4,5,18,19]. To enhance the efficiency of thermoelectric conversion, a central focus in thermoelectric materials research has been to reduce irreducible thermal transport while simultaneously maintaining exceptional electrical transport properties [8,20]. Many halide perovskites have been observed to exhibit remarkably low thermal conductivities in experimental measurements [2,4,5,21,22], owing to their soft lattice structures and strong anharmonicity. For instance, Pisoni *et al.* [21] first reported an ultra-low room-temperature thermal conductivity of $0.5 \text{ Wm}^{-1}\text{K}^{-1}$ in hybrid inorganic-organic halide perovskite $\text{CH}_3\text{NH}_3\text{PbI}_3$, which was attributed to the dynamic cation disorder and an expected soft lattice. Lee *et al.* [4] experimentally reported an ultra-low thermal conductivity of 0.45 and $0.42 \text{ Wm}^{-1}\text{K}^{-1}$ for all-inorganic halide perovskite CsPbI_3 and CsPbBr_3 , respectively, which can be traced back to the highly anharmonic cluster rattling. Acharyya *et al.* [5] first experimentally observed an ultra-low thermal conductivity of $\sim 0.37\sim 0.28 \text{ Wm}^{-1}\text{K}^{-1}$ in the temperature range of 295~523 K, which is originated from the

anharmonic soft vibrations of sublattice. Although the significant research progress of physical properties in halide perovskites, the environmental toxicity of the Pb ion and poor thermal and chemical stabilities remain a limitation for large-scale commercialization for all-inorganic lead halide perovskites [23] and organic-inorganic halide perovskites [24], respectively.

Recently, nontoxic and highly stable low-dimensional Cu halides have been attracting growing interest due to their distinctive physical properties such as high photoluminescence quantum efficiencies and widely adjustable emission wavelengths [25,26]. Prominent instances encompass $\text{Cs}_3\text{Cu}_2\text{X}_5$ (quasi-zero dimensional (0D)) [27,28], Rb_2CuX_3 (quasi-1D) [29], and CsCu_2X_3 [26,30,31] (quasi-1D), with X representing Cl, Br, and I. Extensive research has been conducted on the favorable optical characteristics of these metal halides [26,30-33], which are primarily attributed to the presence of robust self-trapped excitons resulting from their reduced dimensionality [34]. Despite considerable efforts on opto-electronic properties of low-dimensional metal halides, the lattice dynamics and thermal transport impacting their optoelectronic properties are yet to be further explored. Theoretical investigations into the thermal conductivity of $\text{Cs}_3\text{Cu}_2\text{X}_5$ (quasi-0D) [35] and CsCu_2X_3 [36] have been carried out, revealing remarkably low thermal conductivity values of 0.018 and $0.05 \text{ Wm}^{-1}\text{K}^{-1}$ at room temperature, respectively. However, these ultralow thermal conductivities were calculated using the lowest order of perturbation theory, considering only three-phonon scattering processes, a single particle-like phonon propagation channel, and 0-K harmonic phonons. Lattice vibrations in functional materials often display strong anharmonicity [37]. Consequently, the quasi-harmonic phonon theory, which doesn't account for temperature-dependent anharmonic interactions, fails to capture their lattice dynamics, particularly for optoelectronic and photovoltaic materials [19,36-38]. In these scenarios, it is essential to go beyond three-phonon scattering processes, as higher-order phonon scattering can play a significant role in

determining the lattice thermal conductivity in highly anharmonic compounds. This phenomenon is evident in materials such as AgCrSe_2 [39], $\text{Cu}_{12}\text{Sb}_4\text{S}_{13}$ [40], and Tl_3VSe_4 [41]. Furthermore, materials exhibiting ultra-low thermal conductivity approaching the glass limit may challenge the effectiveness of the conventional Peierls-Boltzmann transport equation (PBTE) method [42] for explaining thermal transport [4,43-45]. In such cases, both the wave-like and particle-like characteristics of phonons may play pivotal roles in the thermal transport process [40,43-47]. Therefore, a thorough comprehension of the lattice dynamics and the microscopic mechanisms governing thermal transport in low-dimensional metal halides remains largely uncharted territory, presenting an urgent need for potential thermoelectric applications.

In this work, we thoroughly investigate the anharmonic lattice dynamics and the microscopic mechanisms of thermal transport in the quasi-1D copper halide CsCu_2I_3 by using a state-of-the-art first-principles scheme. Within this first-principles-based framework, we combine the anharmonic phonon renormalization technique and a unified theory of thermal transport to calculate the lattice thermal conductivity of CsCu_2I_3 . To accurately capture the lattice dynamics and thermal transport characteristics, both the 3ph and 4ph scatterings are considered in self-consistent phonon calculations and dual-channel thermal transport mode, i.e., particle-like phonon propagation and wave-like tunnelling of phonons. At zero-K phonon calculations, we observe that the CsCu_2I_3 structure with a *cmcm* space group exhibits dynamical instability. However, it can be anharmonically stabilized at ~ 75 K, suggesting that it represents a low-temperature average structure. Furthermore, we demonstrate that the unique chain-like 1D structure leads to low-lying flat modes in mid-frequency region, consequently resulting in dramatically strong 4ph scattering rates in crystalline CsCu_2I_3 . Using the dual-channel transport model, we show the effect of 4ph scatterings on particle-like phonon propagation and wave-like tunnelling of phonons and predicted

an ultra-low thermal conductivity for CsCu₂I₃. We find that the conventional phonon-gas model fails to explain the thermal transport in cooper halide CsCu₂I₃. Particularly, the cross-chain thermal conductivity exhibits an abnormal upward trend with increasing temperature and this behavior is primarily attributed to the dominance of wave-like tunnelling of phonons in cross-chain thermal transport. Our work reveals the anomalous heat conduction physics in crystalline CsCu₂I₃, which also helps to understand thermal transport of other quasi-1D materials with ultra-low thermal conductivity.

II. COMPUTATIONAL DETAILS AND METHODOLOGY

First-principles calculations and compressive Sensing technique

Density functional theory (DFT) calculations for the CsCu₂I₃ crystal were carried out using projector-augmented wave (PAW) [48] pseudopotentials, which were implemented in the Vienna Ab initio Simulation Package (VASP) [49]. PAW pseudopotentials were employed to treat the Cs(5s²5p⁶6s¹), Cu(3d¹⁰4s¹) and I(4d¹⁰ 5s² 5p⁵) shells as valence electrons and the PBEsol [50] of the generalized gradient approximation (GGA) [51] was utilized to the exchange-correlation functional in all calculations. A kinetic energy cut-off value of 520 eV and a 10×10×8 Monkhorst-Pack electronic k -point grid were used for structural optimization of primitive cell. Tight force and energy convergence criterions were set to 10⁻⁵ eV·Å⁻¹ and 10⁻⁸ eV, respectively, for both structural relaxation and self-consistent DFT calculations. The fully optimized lattice constants ($a = 10.063$, $b = 13.082$ Å, $c = 6.104$ Å) agree well with the experimentally reported values ($a = 10.548$ Å, $b = 13.173$ Å, $c = 6.097$ Å) for crystal with a *cmcm* space group [26,52].

The 0-K harmonic (2nd-order) interatomic force constants (IFCs) were extracted using the finite-displacement method [53], as implemented in Phonopy [54]. A 3×3×2 supercell containing 216 atoms was adopted to achieve good convergence for phonon dispersions, wherein a 3×3×4

Monkhorst-Pack electronic k -point grid and a kinetic energy cutoff of 520 eV were used in static DFT calculations. To map out the potential energy surfaces (PESs) for specific phonon modes, the same supercell dimension and input setting of the static self-consistent DFT calculation were employed.

To accurately and efficiently obtain the anharmonic interatomic force constants (IFCs), we opted for the Compressive Sensing Lattice Dynamics method (CSLD) [55] instead of the traditional finite-displacement approach [53]. In particular, we applied the compressive sensing technique [56] of CSLD to identify and collect the physically significant anharmonic IFCs from the extensive set of irreducible anharmonic IFCs, utilizing a constrained displacement-force dataset [57]. Using the random number method, we generated a set of 100 atomic structures directly from an equilibrium $3\times 3\times 2$ supercell. These structures were created along random directions, with a uniform displacement of 0.15 Å applied to all atoms. Subsequently, we conducted a DFT calculation for the 100 atomic structures to acquire the atomic forces. In this calculation, we employed a $3\times 3\times 4$ Monkhorst-Pack electronic k -point grid and set the energy convergence criterion at 10^{-8} eV. In the final step, we utilized the displacement-force datasets and the 0-K harmonic interatomic force constants (IFCs) obtained to extract anharmonic IFCs up to the fourth order. This extraction was accomplished using the least absolute shrinkage and selection operator (LASSO) technique [58]. For the cubic and quartic IFCs extraction, we applied real-space cutoff radii of 7.41 Å and 5.30 Å, respectively. In this work, the IFCs estimation was performed by using the **ALAMODE** package [57,59] and our in-house code **Pheasy** [60].

Anharmonic phonon energy renormalization technique

We compute the anharmonically renormalized phonon energy at finite temperatures using the self-consistent phonon approximation (SCP) [57,61,62]. When considering only the first-order

contribution to the phonon self-energy from quartic anharmonicity, the resulting diagonal SCP equation is expressed as follows:

$$\Omega_q^2 = \omega_q^2 + 2\Omega_q I_q, \quad (1)$$

where ω_q is the zero-K phonon frequency of phonon mode q obtained from harmonic approximation, and Ω_q is the renormalized phonon frequency including temperature effects. The quantity I_q is defined as

$$I_q = \frac{1}{8N} \sum_{q'} \frac{\hbar V^{(4)}(q; -q; q'; -q')}{4\Omega_q \Omega_{q'}} [1 + 2n(\Omega_{q'})], \quad (2)$$

where N is the total number of sampled wave vectors, \hbar is the reduced Planck constant, n is the phonon population from the Bose-Einstein distribution and $V^{(4)}(q; -q; q'; -q')$ is the reciprocal representation of fourth-order IFCs. Additionally, to accurately calculate the anharmonically renormalized phonon energy, we also include the off-diagonal terms of the phonon self-energy, i.e., polarization mixing (PM) [57], into the phonon renormalization calculation. In this study, we employed a \mathbf{q} -mesh of $3 \times 3 \times 2$ for the SCP calculations, which aligns with the dimensions of a $3 \times 3 \times 2$ supercell utilized in the real-space-based phonon energy renormalization technique. Additionally, the SCP \mathbf{q} -mesh of $3 \times 3 \times 2$ was chosen to match the supercell dimensions relevant to the extraction of second-order IFCs in real space.

The anharmonically renormalized phonon energies, resulting exclusively from quartic anharmonicity, may be overestimated for highly anharmonic materials such as BaZrO₃ [63], Cu₁₂Sb₄S₁₃ [40] and Cs₂AgBiBr₆ [38]. As a result, we also take into account the negative energy shifts from bubble diagram due to cubic anharmonicity in addition to the above renormalized phonon energies. The resulting SCP calculation, enhanced by the inclusion of the bubble diagram correction and referred to as SCPB, is defined as [37]

$$\left(\Omega_q^B\right)^2 = \Omega_q^2 - 2\Omega_q \text{Re} \sum_q^B [G, \Phi_3](\Omega = \Omega_q^B), \quad (3)$$

where B stands for the bubble diagram, Φ_3 is the third-order IFCs explicitly included in the anharmonic self-energy calculation, and $\sum_q^B [G, \Phi_3](\Omega_q)$ is the frequency-dependent phonon bubble self-energy. In this study, the anharmonic phonon renormalization was performed using the **ALAMODE** package [37,57]. Within the framework of the quasiparticle (QP) approximation, several treatment options, including QP[0], QP[S], and QP-NL, can be selected to solve Eq. (3) and obtain the fully renormalized phonon energies accounting for cubic and quartic anharmonicities [37]. Following the recommendation in the literature [37], we opted for the QP-NL treatment to evaluate the negative phonon energy shifts resulting from the bubble diagram. Furthermore, we ignore the minor phonon energy shifts caused by the tadpole diagram from cubic anharmonicity, a phenomenon observed in many crystals [40,63,64]. It's worth noting that in this study, we utilized our in-house code for the transformation of force constants between the **ALAMODE** [57,59] and **ShengBTE** [65] packages.

Intrinsic and Extrinsic Phonon Scattering Rates

The intrinsic multi-phonon scattering rates, including both three-phonon (3ph) Γ_q^{3ph} and four-phonon (4ph) Γ_q^{4ph} scattering rates, can be derived from Fermi's golden rule from perturbation theory [66]. Under the single-mode relaxation time approximation (SMRTA) treatment, the Γ_q^{3ph} and Γ_q^{4ph} can be expressed as [40,41,66]

$$\Gamma_q^{3ph} = \sum_{q'q''} \left\{ \frac{1}{2} (1 + n_{q'}^0 + n_{q''}^0) \zeta_- + (n_{q'}^0 - n_{q''}^0) \zeta_+ \right\}, \quad (4)$$

$$\Gamma_q^{4ph} = \sum_{q'q''q'''} \left\{ \frac{1}{6} \frac{n_{q'}^0 n_{q''}^0 n_{q'''}^0}{n_q^0} \zeta_{--} + \frac{1}{2} \frac{(1 + n_{q'}^0) n_{q''}^0 n_{q'''}^0}{n_q^0} \zeta_{+-} + \frac{1}{2} \frac{(1 + n_{q'}^0)(1 + n_{q''}^0) n_{q'''}^0}{n_q^0} \zeta_{++} \right\}, \quad (5)$$

where the phonon mode q is a composite index of the wavevector \mathbf{q} and phonon branch j , and n is the phonon population from the Bose-Einstein distribution, with

$$\zeta_{\pm} = \frac{\pi\hbar}{4N} \left| V^{(3)}(q, \pm q', -q'') \right|^2 \Delta_{\pm} \frac{\delta(\Omega_q \pm \Omega_{q'} - \Omega_{q''})}{\Omega_q \Omega_{q'} \Omega_{q''}}, \quad (6)$$

and

$$\zeta_{\pm\pm} = \frac{\pi\hbar^2}{8N^2} \left| V^{(4)}(q, \pm q', \pm q'', -q''') \right|^2 \Delta_{\pm\pm} \frac{\delta(\Omega_q \pm \Omega_{q'} \pm \Omega_{q''} - \Omega_{q'''})}{\Omega_q \Omega_{q'} \Omega_{q''} \Omega_{q'''}}}, \quad (7)$$

Where $V^{(3)}(q, \pm q', -q'')$ and $V^{(4)}(q, \pm q', \pm q'', -q''')$ are the reciprocal representation of 3rd- and 4th-order IFCs, respectively [65,67], the delta function $\delta(\Omega)$ is enforced to ensure energy conservation in both 3ph and 4ph scatterings, and the Kronecker deltas Δ_{\pm} and $\Delta_{\pm\pm}$ are enforced to ensure momentum conservation for 3ph and 4ph scattering processes, respectively.

The extrinsic phonon scatterings from isotopes, denoted as $\Gamma_q^{isotope}$, can be expressed as [68]

$$\Gamma_q^{isotope} = \frac{\pi\Omega_q^2}{2N} \sum_{i \in u.c.} g(i) \left| e_q^*(i) \cdot e_{q'}(i) \right|^2 \delta(\Omega - \Omega'), \quad (8)$$

where $e_q(i)$ is the eigenfunction of phonon mode q at the atom i , and $g(i)$ is the Pearson deviation coefficient and its detailed expression can be referred to literature [68].

By combining the intrinsic and extrinsic phonon scattering rates and applying Matthiessen's rule, the total phonon scattering rate Γ_q can be expressed as

$$\Gamma_q = \Gamma_q^{3ph} + \Gamma_q^{4ph} + \Gamma_q^{isotope}, \quad (9)$$

Unified Theory of Thermal Transport

We use a unified theory of thermal transport [46,47] to compute the total lattice thermal conductivity κ_L . The total κ_L can be obtained by summing the populations' contribution κ_L^P and

coherences' contribution κ_L^C , namely $\kappa_L = \kappa_L^P + \kappa_L^C$, where κ_L^P and κ_L^C account for the diagonal and off-diagonal terms of heat flux operators, respectively. Specifically, κ_L^P and κ_L^C arise from the particle-like phonon propagation and wave-like tunnelling of phonons, respectively. The detailed formula for $\kappa_L^{P/C}$ under the SMRTA can be expressed as [46,47]

$$\kappa_L^{P/C} = \frac{\hbar^2}{k_B T^2 V N} \sum_{\mathbf{q}} \sum_{j,j'} \frac{\Omega_{\mathbf{q}j} + \Omega_{\mathbf{q}j'}}{2} \mathbf{v}_{\mathbf{q}j'} \otimes \mathbf{v}_{\mathbf{q}j} \cdot \frac{\Omega_{\mathbf{q}j} n_{\mathbf{q}j} (n_{\mathbf{q}j} + 1) + \Omega_{\mathbf{q}j'} n_{\mathbf{q}j'} (n_{\mathbf{q}j'} + 1)}{4(\Omega_{\mathbf{q}j} - \Omega_{\mathbf{q}j'})^2 + (\Gamma_{\mathbf{q}j} + \Gamma_{\mathbf{q}j'})^2} (\Gamma_{\mathbf{q}j} + \Gamma_{\mathbf{q}j'}) , \quad (10)$$

where k_B , T , V and \mathbf{v} are, respectively, the Boltzmann constant, the temperature in Kelvin, the primitive-cell volume and the group velocity matrix, including both the diagonal and off-diagonal terms [69]. In Eq.(10), when $j = j'$, it results in the populations' contribution (PBTE result) (κ_L^P), otherwise, it gives the coherences' contribution (κ_L^C). In solving Eq. (10), we used a \mathbf{q} mesh of $9 \times 9 \times 13$ for the 3ph and 4ph scattering processes, with scalebroad parameters set at 0.5 and 0.02, respectively. These parameter choices resulted in well-converged results for the CsCu₃I₂ crystal. Additionally, the iterative scheme for the PBTE is exclusively applied to handle 3ph scattering processes. In contrast, the treatment of 4ph scattering processes is conducted at the SMRTA level due to the exceptionally high memory demands [40,67]. In this work, thermal conductivity calculations, including populations' and coherences' contributions, were carried out using the **ShengBTE** [65] and **FourPhonon** [67] packages, and our in-house code [38,63].

III. RESULTS AND DISCUSSIONS

a) Crystal Structure, Phonon Dispersions and Lattice Anharmonicity

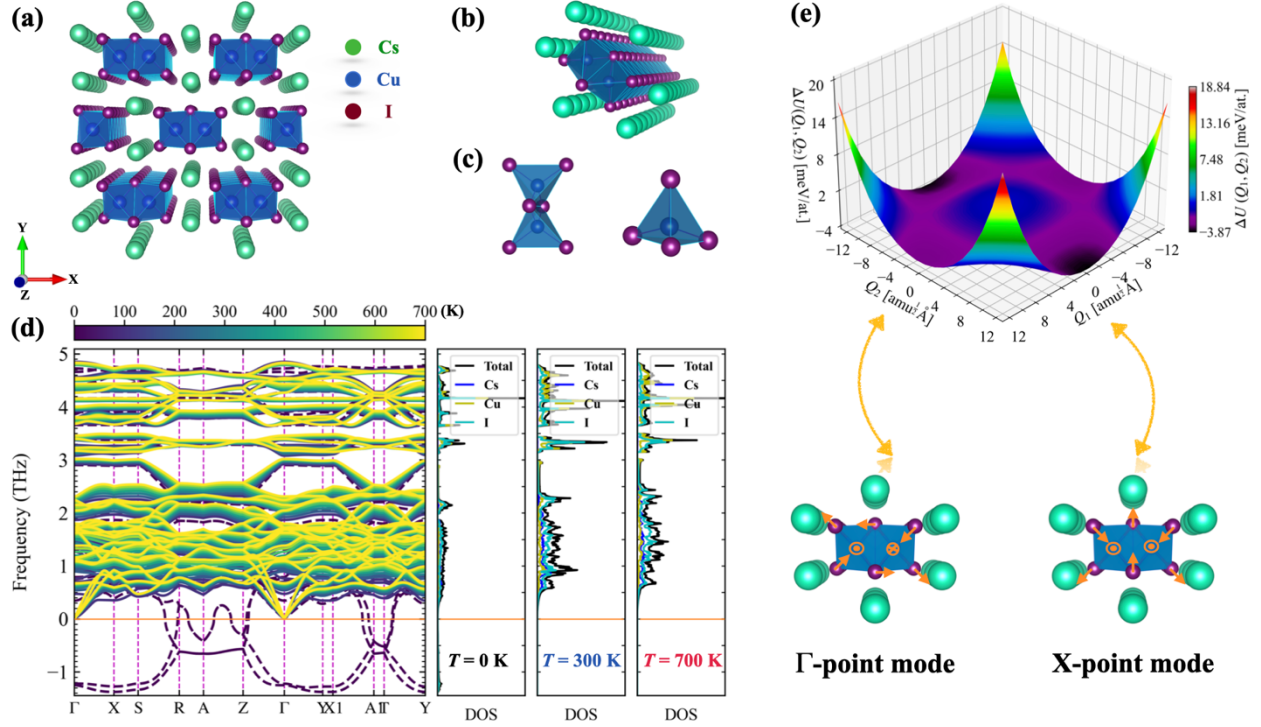


FIG. 1. (a) Crystal structure of cubic copper halide CsCu_2I_3 , which features one-dimensional (1D) Cu-I chains surrounded by Cs atoms. (b) A perspective view of the 1D polyanionic $[\text{Cu}_2\text{X}_3]^-$ chain with loosely bounded Cs atoms, wherein the polyanionic $[\text{Cu}_2\text{X}_3]^-$ units are formed by edge-shared connection of Cu_2X_3 tetrahedra. (c) Polyanionic $[\text{Cu}_2\text{X}_3]^-$ polyhedron and Cu_2X_3 tetrahedra, respectively. (d) Calculated anharmonically renormalized phonon dispersions at finite temperatures (from 100 to 700 K) compared with phonon dispersions computed by harmonic approximation treatment at 0 K. The calculated atom-decomposed partial and total phonon densities of states (DOS) at 0, 300 and 700 K are shown on the right panel, respectively. (e) Calculated two-dimensional (2D) potential energy surface of CsCu_2I_3 as a function of normal mode coordinates Q_1 and Q_2 . Here the soft modes at the Γ and X points are associated with the vibrations of Cu and I atoms and these vibrational animations are denoted by arrows and in/out circles.

We start by analyzing the anharmonic lattice dynamics of the 1D CsCu_2I_3 crystal structure at finite temperatures, as illustrated in Fig. 1. In Figures 1(a-c), Cu^+ ions occupy the interstitial sites in the tetrahedrally coordinated sublattice formed by Γ^- anions, resulting in the formation of $[\text{CuI}_4]^{3-}$ units. The paired $[\text{CuI}_4]^{3-}$ tetrahedral strings, nestled within rhombic columnar cages formed by Cs^+ cations, stack infinitely via edge sharing, giving rise to the $[\text{Cu}_2\text{I}_3]^-$ anionic chains of CsCu_2I_3 , as shown in Figs. 1(b-c) [26,32]. Furthermore, previous study had revealed that the orbitals of Cu and I atoms predominantly influence the valence and conduction band minimum, indicating that Cs^+ cations serve as a quasi-isolating shell for the 1D $[\text{Cu}_2\text{I}_3]^-$ chains [32].

Next, we calculate the vibrational properties of the 1D copper halide CsCu_2I_3 using the harmonic approximation (HA) approach [42]. In Fig. 1(d), phonon softening is evident across the entire Brillouin zone, indicating the dynamical instability of CsCu_2I_3 at low temperatures, a result consistent with prior calculation [36]. The soft modes predominately arise from both Cu and I atoms, as evidenced by the atom-decomposed partial DOS in the right panel of Figure 1(d) and the projected atomic participation ratio (see Fig. S1(a-d) in the supplementary material (SM) [70]). To account for temperature effect on phonons in CsCu_2I_3 , we consider both cubic and quartic anharmonicities in the phonon energy renormalization. Particularly, the cubic anharmonicity contributes to the negative phonon energy shifts, which is found to be crucial for predicting anharmonic phonon behavior in highly anharmonic compounds [37,40,71,72]. After anharmonic phonon renormalization, we observe a substantial stiffening of the soft modes with increasing temperature, as shown in Fig. 1(d). Furthermore, it's noteworthy that all anharmonically renormalized phonons exhibit stabilization above 75 K, as illustrated in Fig. S2 (a-c) of the SM [70]. This relatively low phase transition temperature provides an explanation for the experimentally observed CsCu_2I_3 structure, characterized by a *cmcm* space group at room temperature [26,32,52]. In addition to the Cu/I-dominated soft modes, the low-frequency optical modes (≤ 2.5 THz), mainly contributed by I atoms, also experience a progressive stiffening [see Figs. 1(d) and S1(a,c) in the SM [70]]. In the low-frequency regime, phonon modes primarily dominated by Cs atoms exhibit behavior similar to the rattler-like modes observed in caged compounds [61,73,74]. The rattling motion of these modes is demonstrated by the small atomic participation ratio and their temperature-dependent phonon stiffening is attributed to the large mean-square atomic displacements (MSD) of Cs atoms [see Figs. S3-4 in the SM [70]]. Conversely, the high-frequency phonon modes (> 2.5 THz) in CsCu_2I_3 are primarily dominated by the

relatively light Cu atoms, as depicted in Figs. S1(a) and (d) in the SM [70]. These modes display a minor or negligible temperature-dependent stiffening, akin to the high-frequency phonon behavior observed in compounds like BaZrO₃ [63] and others [64].

To gain a more profound understanding of lattice anharmonicity and instability in the CsCu₂I₃ crystal, we construct a 2D potential energy surface (PES) [75] for the soft modes at the Γ and X points in Fig. 1(e). As expected, the minimum energy is situated beyond the zero-tilt amplitude ($Q_1 = Q_2 = 0$) for both soft modes at the Γ and X points, respectively, indicating strong lattice anharmonicity and dynamical instability [see Fig. 1(e)]. The soft modes at the Γ and X points are exclusively linked to the lattice vibrations of the 1D [Cu₂I₃]⁻ chains, despite the fact that the Cs atoms exhibit the largest MSD [see Figs. 1(e) and S2 of the SM [70]]. In this context, the out-of-plane motions are attributed to I atoms, while the in-plane motions are assigned to Cu atoms, as illustrated in Fig. 1(e). Evidently, the source of lattice instability in CsCu₂I₃ differs from that in double perovskite [19,38], where the rotational sublattice causes the lattice instability. Although the minimum energies are located beyond the zero-tilt amplitude for both soft modes, it's important to highlight that these minima are relatively shallow, predicting approximately -2.57 and -3.91 meV/atom, respectively. This observation suggests that the high-temperature phase of CsCu₂I₃ crystal effectively represents an averaged structure at relatively low temperatures, analogous to compounds like CsSnI₃, CsSnBr₃ and CsSnCl₃ [76,77].

b) Bond strength and phonon group velocity

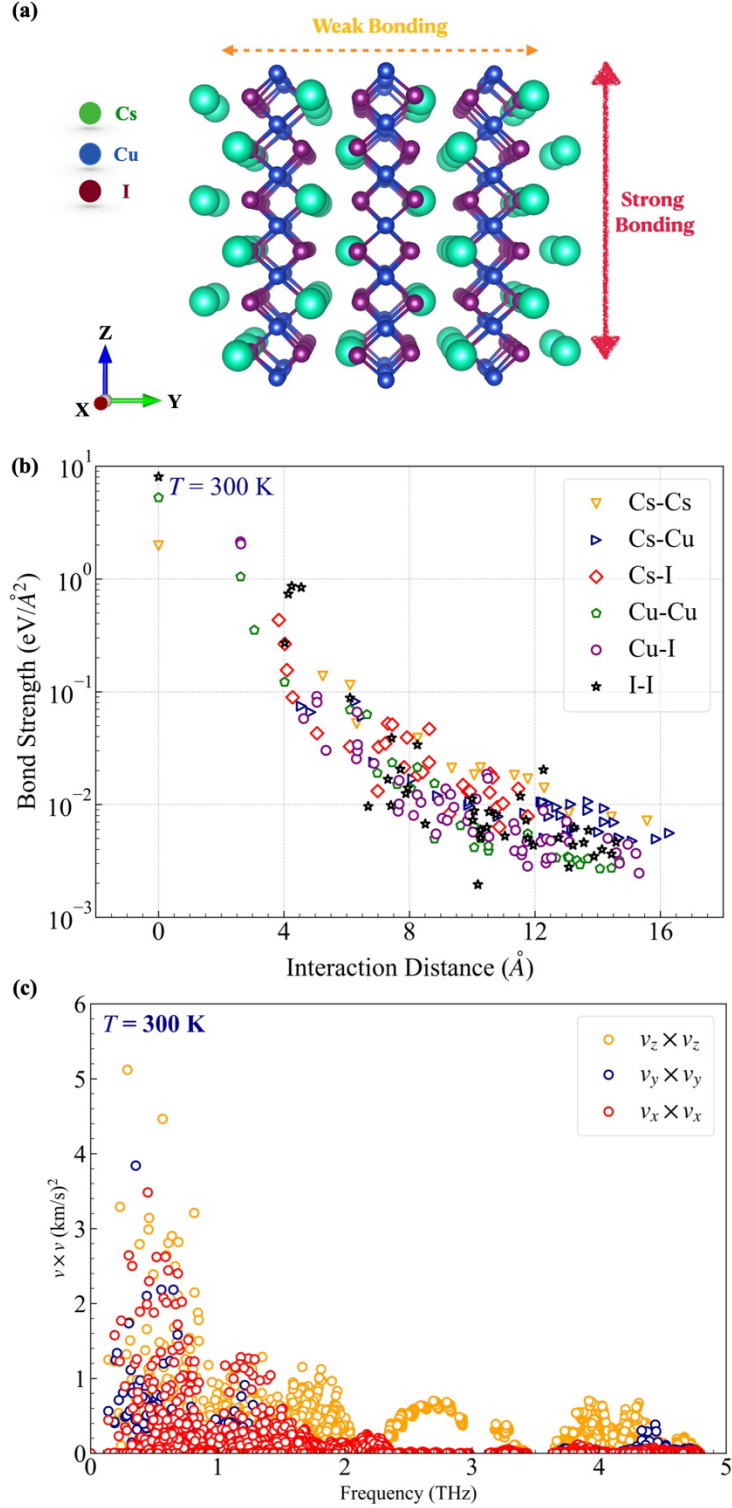


FIG. 2. (a) A perspective view of Cubic copper halide CsCu_2I_3 projected along the X axis. (b) Calculated bond strength as a function of interaction distance of atomic pairs at 300 K. (c) Calculated phonon group velocities along x, y and z axis, respectively, using the finite-temperature second-order interatomic force constants at 300 K.

Considering the crucial role of bond strength in characterizing thermal transport in compounds [78,79] we now turn our attention to the examination of bond strengths and group velocities in crystalline CsCu_2I_3 . Given the unique chain-like structure of CsCu_2I_3 , we expect strong bonding features along the chain axis, contrasting with weak bonds in the cross-chain directions, as illustrated in Fig. 2(a). From figure 2(b), it is evident that the in-chain bond strengths of nearest-neighbor Cu-I and Cu-Cu pairs exhibit highest values of ~ 2 and 1.05 eV/\AA^2 , respectively. In contrast, small values of ~ 0.4 and 0.08 eV/\AA^2 are observed for the cross-chain bond strengths of nearest-neighbor Cs-I and Cs-Cu pairs, respectively. The weak interaction between Cs and I/Cu atoms is a key factor contributing to the rattling vibrations of Cs atoms in CsCu_2I_3 , consequently leading to small group velocity and strong anharmonicity [5,61,73,80]. Furthermore, the significant differences between the in-chain and cross-chain bond strengths are expected to result in strong anisotropy in group velocity. Indeed, the group velocities along the chain axis (Z-axis) are consistently greater than those in the cross-chain directions (X/Y axes) [see Fig. 2(c)], thus giving rise to anisotropic thermal conductivity. Importantly, in comparison to the group velocities along the chain-axis (Z-axis), the cross-chain (X/Y-axis) group velocities exhibit rapid decay, particularly for phonons with frequencies exceeding 2 THz. We attribute this anomalous phenomenon to the ‘quiescence’ behavior of Cs^+ ion, as evidenced by the PDOS and atomic participation ratio [see Figs. 1(d) and S1(a-d) in the SM [70]]. More specifically, Cs atoms do not participate in the collective vibrations of atoms with frequencies exceeding 2 THz, which impedes the phonon propagation along cross-chain directions [71,81]. The exceptionally low cross-chain group velocities for high-frequency phonons ($> 2 \text{ THz}$) lead to the loss of the phonon quasi-particle picture, thus enhancing the nature of wave-like tunnelling of phonons. Consequently, the distinct

features between chain-axis and cross-chain group velocities may give rise to different mechanisms of thermal transport along those orientations.

c) Phonon scattering rates, phase spaces and lifetimes

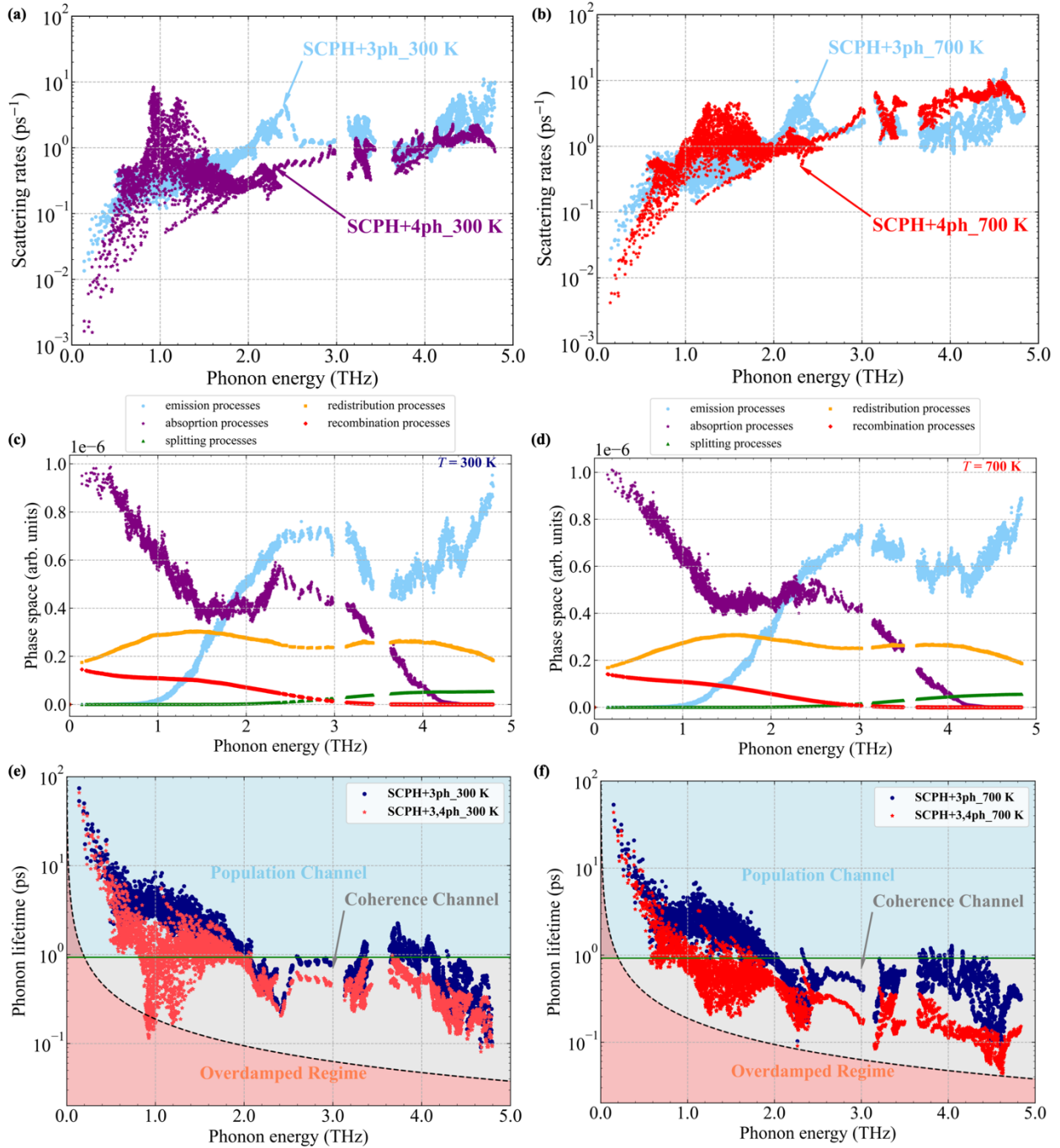


FIG. 3. (a) Calculated three- (3ph) and four-phonon (4ph) scattering rates at 300 K using anharmonically renormalized phonon frequencies and eigenvectors. (b) The same as (a), but at 700 K. (c) Calculated scattering phase spaces, including emission and absorption processes for three-phonon scatterings as well as splitting, redistribution and recombination processes for four-phonon scatterings at 300 K. (d) The same as (c), but at 700 K. (e) Calculated phonon lifetimes for three-phonon scattering processes, as well as for both the three- and four-phonon scattering processes at 300 K using anharmonically renormalized phonon frequencies and eigenvectors. The horizontal green solid line represents the Wigner limit in time [47]. Phonons with a lifetime above this limit primarily contribute to the populations' thermal conductivity κ_L^P , while those below mainly contribute to coherences' thermal conductivity κ_L^C . The dashed black curve depicts the Ioffe-Regel limit in time [82]. Phonons with a lifetime larger than the Ioffe-Regel limit are considered well-defined, whereas those below are recognized as overdamped. (f) The same as (e), but at 700 K.

Taking into account the strong anharmonicity in CsCu₂I₃ crystal, we explicitly incorporate both cubic and quartic anharmonicities into phonon scattering rates for the determination of thermal conductivity κ_L [42,67]. In Figs. 3(a) and 3(b), we compute the 3-phonon (3ph) and 4-phonon (4ph) scattering rates by using anharmonically renormalized phonon modes alongside the 3rd and 4th force constants at temperatures of 300 and 700 K, respectively. We observe that at 300 K, Γ_{4ph} surpasses Γ_{3ph} for modes with frequencies in the 0.5 to 1.5 THz range, which shifts to 0.6–1.8 THz at 700 K [see Figs. 3(a-b)]. Obviously, the 4ph interaction processes not only play a crucial role in accurately predicting finite-temperature phonon energies but also determining thermal transport for CsCu₂I₃ crystal. Additionally, the Γ_{4ph} within the mentioned frequency interval undergoes a sudden increase, while Γ_{3ph} does not demonstrate a similar abrupt rise. Meanwhile, we observe a direct correlation between the peak of the 4ph scattering rates and the temperature-dependent shift in Cs-dominated phonons [see Figs. 1(d), 3(a-b) and S1(d)]. Hence, we attribute the abrupt rise in 4ph scattering rates to the presence of Cs-dominant rattling modes, i.e., low-lying flat modes. This phenomenon is not observed in frequency regions where Cs atoms are not involved [see Figs. 1(d), 3(a-b) and S1(a-d) in the SM [70]]. Similarly, the low-lying flat phonon modes consistently exhibit high phonon scattering rates in many crystals, including Cu₁₂Sb₄S₁₃ [40], Ba₈Ga₁₆Ge₃₀ [73], AgCrSe₂ [39] and YbFe₄Sb₁₂ [64,80]. The quasi-one-dimensional, chain-like structure of crystalline CsCu₂I₃ induces rattling vibrations of Cs atoms, consequently leading to the prevalence of

dominant 4ph scattering rates. Interestingly, it's worth noting that the 3ph scattering phase spaces are generally larger than the 4ph phase spaces, implying that the significant 4ph scattering rates result from the extensive 4ph scattering matrices [see Figs. 3(c-d)]. This differs from observations in materials such as $\text{Cu}_{12}\text{Sb}_4\text{S}_{13}$ [40] and $\text{Ba}_8\text{Ga}_{16}\text{Ge}_{30}$ [73].

Recently, Simoncelli *et al.* [46,47] have introduced a novel parameter, i.e., the Wigner limit in time, for characterizing phonons in compounds with complex structures or/and strong anharmonicity. This parameter aids in categorizing phonons into distinct thermal transport regimes, where they are either dominated by particle-like phonon propagation or wave-like tunnelling of phonons channels. The Wigner limit in time is defined as $\tau = 3N_{at}/\omega_{max}$, where N_{at} is the number of atoms in the primitive cell and ω_{max} is the maximum phonon frequency. In Figs. 3(e-f), when considering only 3ph scattering processes, it becomes apparent that most phonons with frequencies exceeding 2 THz are located below the Wigner limit in time. This observation underscores the importance of coherence channel (wave-like tunnelling of phonons) in thermal transport of crystalline CsCu_2I_3 . Nonetheless, the lifetimes of phonons with frequencies below 2 THz, which serve as the principal heat carriers, still exceed the Wigner time limit. This suggests that perhaps the population channel, i.e., particle-like phonon propagation, continues to govern thermal transport. The inclusion of additional 4ph scattering processes leads to a significantly increased population of phonons with lifetimes lower than the Wigner limit in time [see Fig. 3(e-f)]. Notably, a substantial proportion of phonons with frequencies less than 2 THz dip below the Wigner time limit, some even approaching the overdamped region. This observation emphasizes the significance of the strong 4ph scatterings induced by the chain-like structure of CsCu_2I_3 in accurately unveiling the mechanisms of thermal transport. It also implies that the coherence

channel probably holds a dominant role in thermal transport in crystalline CsCu_2I_3 , as depicted in Figs. 3(e-f).

d) Cumulative and Spectral thermal conductivity

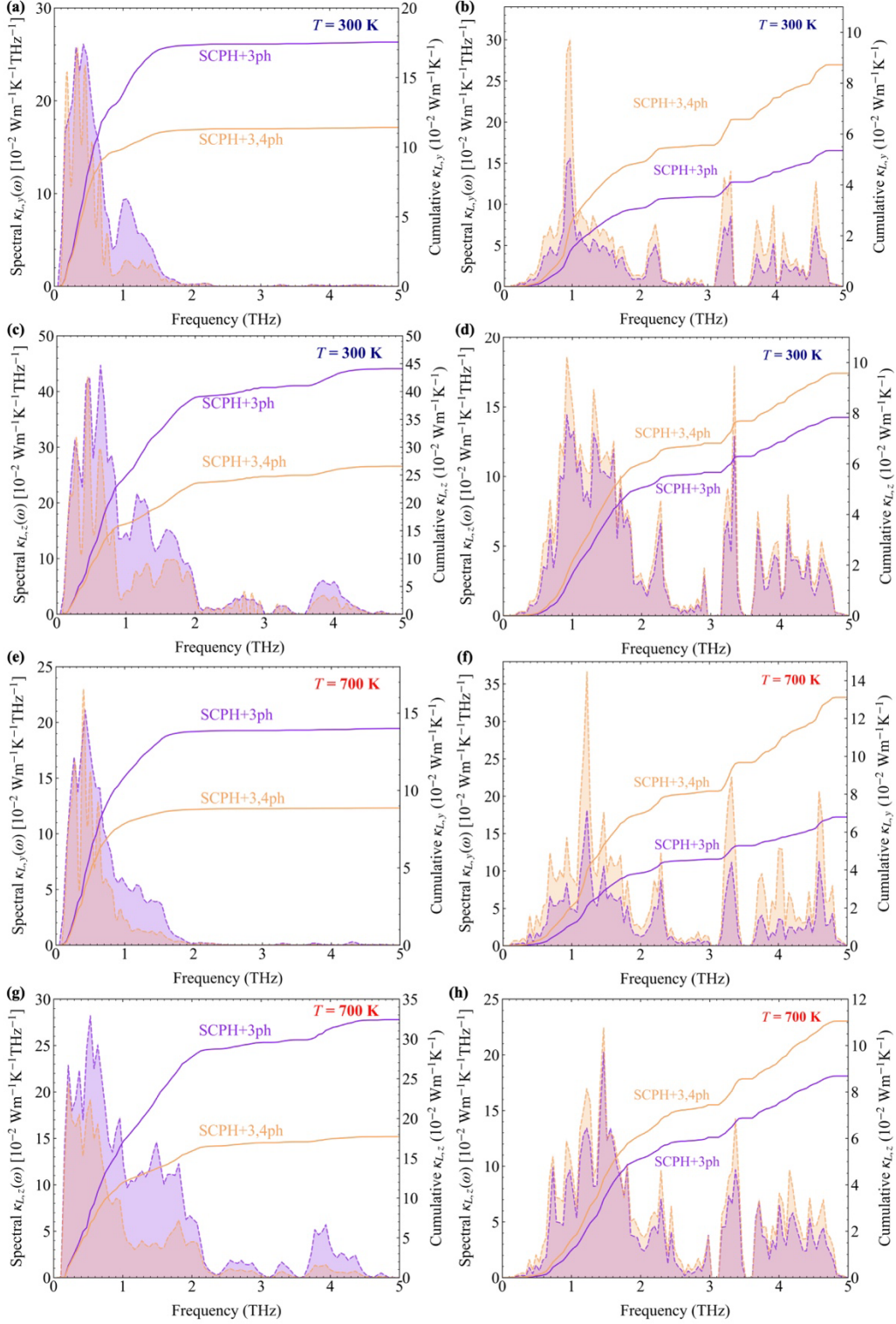


FIG. 4. Comparison of spectral/cumulative populations' and coherences' thermal conductivity obtained with (SCPH+3,4ph model) or without (SCPH+3ph model) 4ph scattering rates 300 and 700K, respectively. (a) Spectral and cumulative populations' thermal conductivity along the y axis obtained at 300 K. (b) Spectral and cumulative coherences' thermal conductivity along the y axis obtained at 300 K. (c) The same as (a), but along the z axis. (d) The same as (b), but along the z axis. (e) The same as (a), but at 700 K. (f) The same as (b), but at 700 K. (g) The same as (e), but along the z axis. (h) The same as (f), but along the z axis.

We move on to calculate the spectral and cumulative populations' thermal conductivity κ_L^P and coherences' thermal conductivity κ_L^C at 300 and 700 K, respectively, as illustrated in Figs. 4(a-h) and S5(a-b) in the SM [70]. Overall, on top of the thermal conductivities obtained considering only 3ph scattering processes, the inclusion of 4ph scattering processes leads to a decrease in κ_L^P but an increase in κ_L^C [40,63]. Furthermore, the chain-axis thermal conductivity $\kappa_{L,z}^P$ is approximately twice that of the cross-chain thermal conductivity $\kappa_{L,x}^P$, whether or not we consider 4ph scatterings, at both 300 K and 700 K [see Figs. 4(a, c, e, g)]. The remarkable anisotropy in particle-like phonon thermal transport observed in crystalline CsCu₂I₃ can be traced back to the unique chain-like 1D structure, which induces significant anisotropy in group velocity [see Fig. 2(c)]. On the contrary, a weak anisotropy is observed between the chain-axis $\kappa_{L,z}^C$ and cross-chain thermal conductivity $\kappa_{L,x}^C$ for crystalline CsCu₂I₃, as shown in Figs. 4(b, d, f, h).

We now delve deeper into a more comprehensive understanding of the spectral and cumulative contributions to thermal conductivity, namely κ_L^P for populations and κ_L^C for coherences. Figures 4(a, c, e, g) clearly illustrate that phonons with frequencies less than 2 THz are the primary heat carriers contributing to κ_L^P in both the chain-axis and cross-chain directions. When considering only 3ph scattering processes, an ultra-low κ_L^P of 0.175 (0.44) Wm⁻¹K⁻¹ and 0.14 (0.32) Wm⁻¹K⁻¹ is observed for the cross-chain (chain-axis) direction at 300 and 700 K, respectively. The ultra-low thermal conductivity in CsCu₂I₃ is primarily attributed to its short phonon lifetimes induced by strong anharmonicity. This conclusion is drawn from a comparison of key factors, including group velocity and phonon lifetime [see Figs. 2(c) and 3(a-b)], between crystalline CsCu₂I₃ and Si [83], using the simple kinetic theory of thermal conductivity [79]. By further incorporating 4ph scattering rates, the corresponding predicted κ_L^P decreases to 0.114 (0.266) Wm⁻¹K⁻¹ and 0.089 (0.177) Wm⁻¹K⁻¹ representing approximately a 35% (40%) and

36% (45%) reduction, respectively, as illustrated in Figs. 4(a, c, e, g). The remarkable reduction in κ_L^P due to 4ph scatterings can be attributed to phonons falling within the frequency range of 0.5-2 THz, which aligns with the dominant region of 4ph scattering rates induced by chain-like structure of CsCu₂I₃ [see Figs. 3(a-b) and 4(a, c, e, g)].

For coherences' contributions to thermal conductivity κ_L^C , we predict a value of 0.053 (0.078) Wm⁻¹K⁻¹ and 0.068 (0.087) Wm⁻¹K⁻¹ along the cross-chain (chain-axis) direction at 300 and 700 K, respectively [see Figs. 4(b, d, f, h)]. These coherences' thermal conductivities account for 23.25% (15.06%) and 32.64% (21.17%) of the corresponding total thermal conductivities, namely, $\kappa_L = \kappa_L^C + \kappa_L^P$, respectively. Even though the κ_L^C makes a significant contribution to the total κ_L , the κ_L^P remains the dominant role in thermal transport in CsCu₂I₃ when considering only 3ph scattering processes. Incorporating the additional 4ph scattering effects, the κ_L^C increases to 0.087 (0.096) Wm⁻¹K⁻¹ and 0.131 (0.111) Wm⁻¹K⁻¹ for the cross-chain (chain-axis) direction at 300 and 700 K, respectively. Consequently, the enhanced percentages are 64.15% (23%) and 92.65% (27.58%) at 300 and 700 K, respectively. In contrast to the cause of κ_L^P reduction due to 4ph scatterings, the significant enhancement in κ_L^C resulting from 4ph scattering is attributed not only to phonons within the frequency range of 0.5-2 THz but those in higher frequency ranges [see Figs. 4(b, d, f, h)]. Notably, the enhanced cross-chain $\kappa_{L,x}^C$ due to 4ph scatterings surpasses the corresponding reduced $\kappa_{L,x}^P$ due to 4ph scatterings at 700 K, as illustrated in Figs. 4(e) and (f). This observation indicates that the conventional Peierls-Boltzmann equation [42] is inadequate for accurately describing thermal transport in CsCu₂I₃, especially in the cross-chain direction. The dominance of $\kappa_{L,x}^C$ in the cross-chain thermal conductivity of CsCu₂I₃ can be traced back to its unique chain-like 1D structure. This unique structure, characterized by weak bonding, results in an exceedingly low cross-chain $\kappa_{L,x}^P$, exceptionally small cross-chain group velocities [see Fig. 2(c)], and strong 4ph

scatterings [see Figs. 3(a-b)], all of which collectively facilitate the wave-like tunnelling of phonons. Figures 4(b, d, f, h) also reveal that 4ph scatterings have a more pronounced impact on cross-chain $\kappa_{L,x}^C$ when compared to chain-axis $\kappa_{L,z}^C$. This distinction can be attributed to the strong wave-like nature of phonons due to exceptionally low group velocities along the cross-chain direction. While $\kappa_{L,x}^C$ governs cross-chain thermal transport, $\kappa_{L,z}^P$ continues to dominate the total chain-axis thermal conductivity across the temperature range of 300-700 K. This observation suggests that particle-like phonon propagation governs chain-axis thermal transport, while wave-like tunnelling of phonons dominates cross-chain thermal transport in CsCu₂I₃.

e) The Two-dimensional modal coherences' conductivity

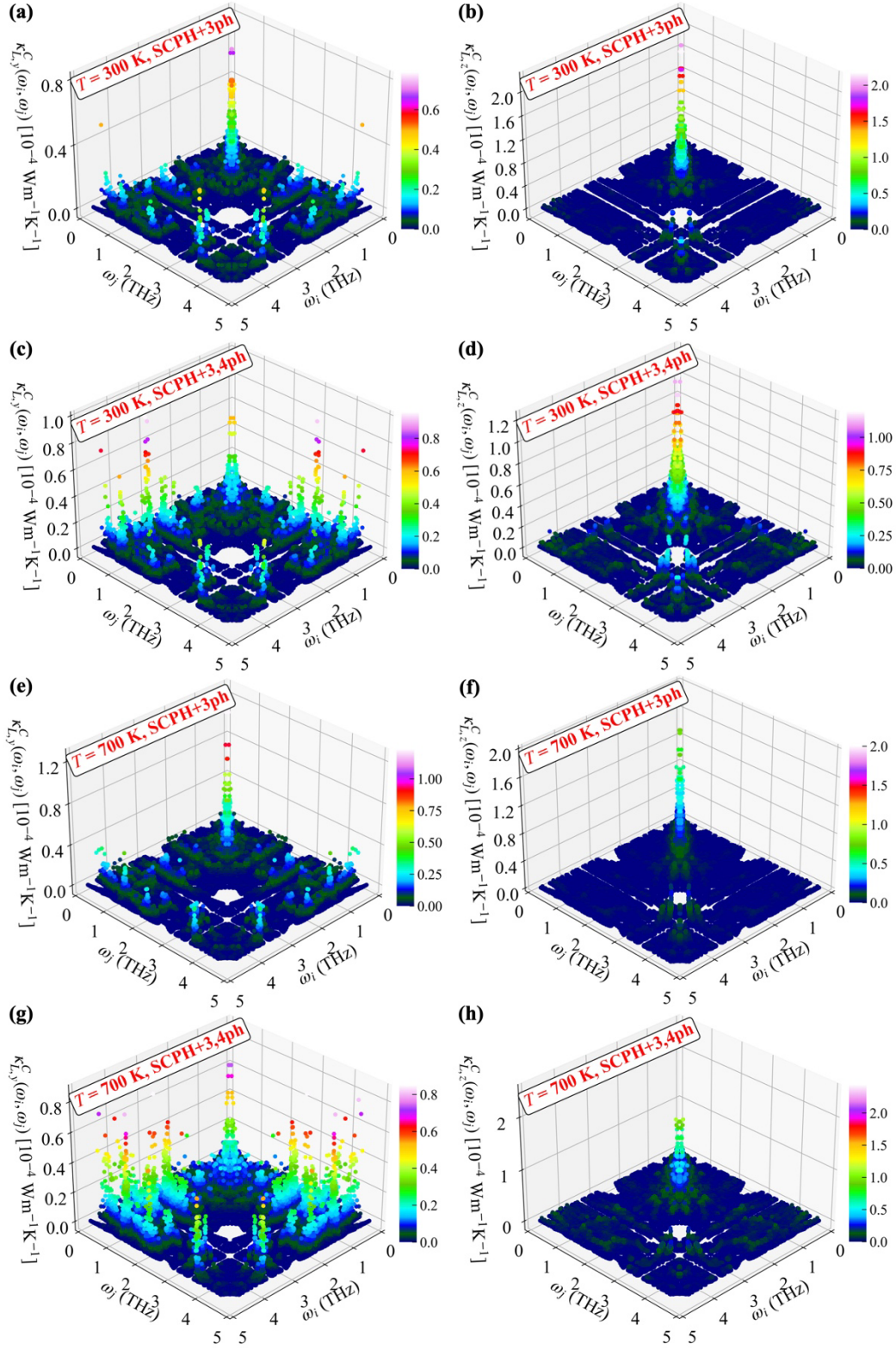


FIG. 5. Calculated Two-dimensional (2D) modal coherences' thermal conductivity $\kappa_L^C(\omega_i, \omega_j)$ obtained with (SCPH+3,4ph model) or without (SCPH + 3ph model) considering 4ph scattering rates at 300 and 700 K, respectively.

(a) Two-dimensional modal $\kappa_{L,y}^C(\omega_i, \omega_j)$ considering only 3ph scattering rates (SCPH+ 3ph model) along the y axis at 300 K. (b) The same as (a), but along the z axis. (c) Two-dimensional modal $\kappa_{L,y}^C(\omega_i, \omega_j)$ considering both 3ph and 4ph scattering rates (SCPH+3,4ph model) along the y axis at 300 K. (d) The same as (c), but along the z axis. (e) Two-dimensional modal $\kappa_{L,y}^C(\omega_i, \omega_j)$ considering only 3ph scattering rates (SCPH+ 3ph model) along the y axis at 700 K. (f) The same as (e), but along the z axis. (g) Two-dimensional modal $\kappa_{L,y}^C(\omega_i, \omega_j)$ considering both 3ph and 4ph scattering rates (SCPH+3,4ph model) along the y axis at 700 K. (h) The same as (g), but along the z axis.

To gain a deeper insight into the wave-like tunnelling of phonons in thermal transport of CsCu₂I₃, we calculate the two-dimensional modal κ_L^C at 300 and 700 K, respectively, as illustrated in Figs. 5(a-h) and S6(a-d). The thermal conductivity κ_L^C , associated with coherences, is determined by the characteristics of two distinct phonons, evaluated through the phonon linewidth and inter-branch spacings [46,47]. In Figs. 5(a-h), when considering only 3ph scatterings, the quasi-degenerate phonon states, namely, two phonons with similar frequencies, exert a predominant influence on both the cross-chain $\kappa_{L,x}^C$ and chain-axis $\kappa_{L,z}^P$ at both 300 and 700 K. With further including 4ph scattering effects, the non-degenerate phonon states start to dominate the cross-chain $\kappa_{L,x}^C$, as illustrated in Figs. 5(c) and (g). This phenomenon can be attributed to the presence of strong 4ph scattering rates (large phonon linewidths), which promote the coupling of two phonons with significantly different frequencies [40,63]. However, the enhancement in chain-axis $\kappa_{L,z}^C$ induced by 4ph scatterings is minor and negligible, as shown in Figs. 5 (d) and (h). The varying effects of 4ph scattering rates on coherences' thermal conductivity along cross-chain and chain-axis directions can be elucidated by the wave-like nature of phonons. The remarkably low group velocities, a consequence of the chain-like structure of CsCu₂I₃, particularly in the high-frequency region, lead to a pronounced wave-like nature of phonons along cross-chain directions. This, coupled with the presence of large phonon linewidths, contributes to the significant cross-chain coherences' conductivity. To be more specific, the couplings between phonons with very different frequencies, such as 1/3.2 THz at 300 K and 1.2/3.3 THz at 700 K, make a noticeable contribution to cross-chain $\kappa_{L,x}^C$ [see Figs. 5(c, g)]. This obvious contribution is a result of the strong wave-like

nature of phonons induced by the exceptionally low group velocities, as illustrated in Fig. 2(c). Conversely, the relatively high group velocities ensure the particle-like nature of phonons along the chain axis, leading to a limited population of phonons with wave-like nature.

f) Temperature-dependent thermal conductivity

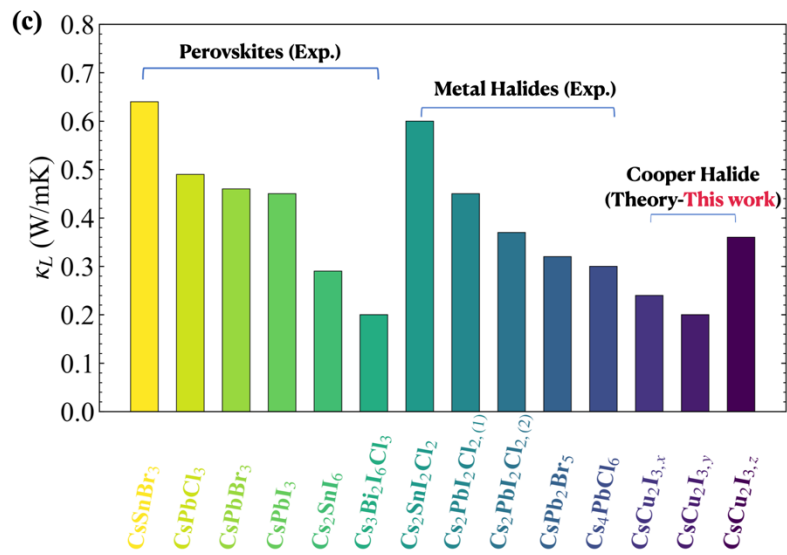
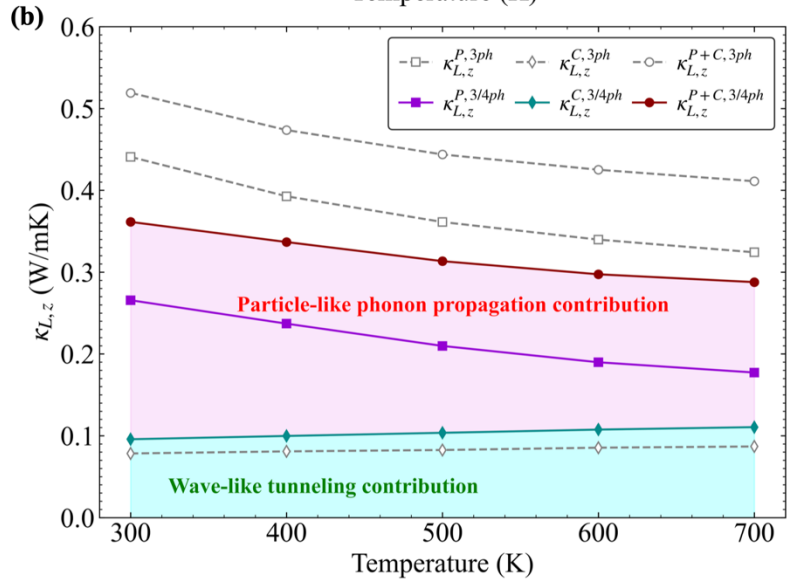
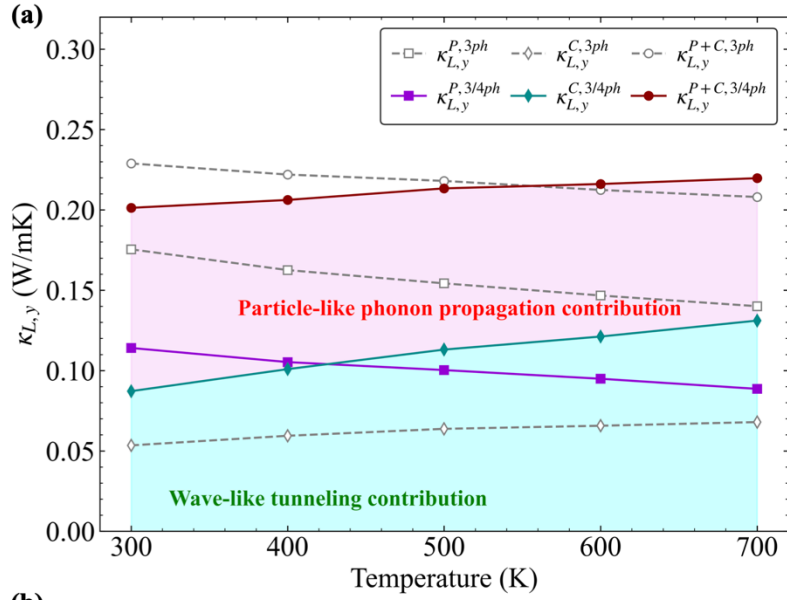


FIG. 6. (a) Calculated temperature-dependent lattice thermal conductivity k_L along the y axis including populations' and coherences' contributions obtained with or without further considering four-phonon scatterings over the temperature range of 300 – 700 K. The pink and light blue shaded areas indicate the contributions from particle-like phonon propagation and wave-like tunnelling of phonons channels, respectively. (b) The same as (a), but along the z axis. (c) Comparison of our predicted lattice thermal conductivity of crystalline CsCu₂I₃ with other experimentally measured ultra-low thermal conductivities of inorganic perovskites and metal halides [2,4,5,22,84-87].

We next move on to examine the temperature dependence of lattice thermal conductivity in crystalline CsCu₂I₃ over the temperature range of 300-700 K, as illustrated in Figs. 6(a-b) and S7 in the SM [70]. When considering only 3ph scatterings, our predicted cross-chain $\kappa_{L,y}^P$ and chain-axis $\kappa_{L,z}^P$ exhibit a weak temperature dependence, roughly proportional to $\sim T^{-0.262}$ and $\sim T^{-0.367}$, respectively. The weak temperature dependences of $\kappa_{L,y}^P$ and $\kappa_{L,z}^P$ contradict the conventional temperature dependence of κ_L^P , which typically follows a $\sim T^{-1}$ relationship [88]. This phenomenon is attributed to anharmonic phonon renormalization, which is also observed materials like BaZrO₃ [63] and double perovskite Cs₂AgBiBr₆ [38]. With the inclusion of the effects of 4ph scatterings, the temperature dependence of $\kappa_{L,y}^P$ and $\kappa_{L,z}^P$ intensifies, now following $\sim T^{-0.283}$ and $\sim T^{-0.483}$, respectively [see Figs. 6(a-b)]. The enhancement in the temperature dependence of κ_L^P can be ascribed to the increase in 4ph scattering rates with increasing temperature, which aligns with prior observations by Feng *et al.* [66] and Zheng *et al.* [63]. In general, the further incorporation of coherences' contribution κ_L^C results in a weaker temperature dependence of the total κ_L . When considering only 3ph scatterings, the temperature dependence of cross-chain $\kappa_{L,y}^P$ changes from $\sim T^{-0.262}$ to $\sim T^{-0.111}$ and chain-axis $\kappa_{L,z}^P$ changes from $\sim T^{-0.367}$ to $\sim T^{-0.279}$. Meanwhile, both cross-chain $\kappa_{L,y}^P$ and chain-axis $\kappa_{L,z}^P$ continue to play their dominant role in the thermal transport of CsCu₂I₃ [see Figs. 6(a-b)]. Interestingly, the inclusion of 4ph scatterings gives rise to distinct behaviors in the chain-axis and cross-chain thermal conductivity of CsCu₂I₃. The total chain-axis $\kappa_{L,z}$ exhibits a relatively mild temperature dependence of $\sim T^{-0.276}$ and show a decreased trend with increasing temperature [see Fig. 6(b)]. In addition, the populations' thermal conductivity from

particle-like phonons still dominates the total chain-axis thermal conductivity $\kappa_{L,z}$. In contrast, the total cross-chain thermal conductivity $\kappa_{L,y}$ displays a highly unusual temperature dependence of $\sim T^{0.106}$, implying that thermal conductivity increases with increasing temperature. This unusual increased trend of cross-chain thermal conductivity is unexpected for single crystal and can be attributed to the dominant role of cross-chain coherences' conductivity in CsCu₂I₃ [see Fig. 6(a)]. Considering the gentle increase in thermal conductivity with rising temperature, we classify it as an atypical glass-like behavior. From Fig. 6(a) we observe that the coherences' conductivity surpasses the populations' conductivity above 422 K. Overall, the chain-like structure of CsCu₂I₃, characterized by cross-chain weak bonding, leads to exceedingly low populations' conductivity and the dominant coherences' conductivity in thermal transport. Consequently, this results in the atypical trend of total cross-chain $\kappa_{L,y}$ increasing with rising temperature.

With the total κ_L in hand, we compare the predicted κ_L of crystalline CsCu₂I₃ with the experimentally measured κ_L of perovskites and metal halides at 300 K [2,4,5,22,84-87], as illustrated in Fig. 6(c). Our predicted room-temperature total κ_L for CsCu₂I₃ is 0.362 Wm⁻¹K⁻¹ for the chain-axis (Z-axis), 0.201 Wm⁻¹K⁻¹ for the cross-chain (Y-axis), and 0.239 Wm⁻¹K⁻¹ for the cross-chain (X-axis), as shown in Figs. 6(a-c) and S7 in the SM [70]. We note that recent theoretical findings have reported record-low lattice thermal conductivities of 0.02 Wm⁻¹K⁻¹ for Cs₃Cu₂I₅ [35] and 0.05 Wm⁻¹K⁻¹ for CsCu₂I₃ with a space group of **Amm2** [36]. We attribute their predicted record-low thermal conductivity to the omission of temperature effects and the neglect of coherences' contributions to thermal conductivity [40,41,46,47,63]. Our theoretical κ_L for crystalline CsCu₂I₃ falls within the range of experimentally measured κ_L for perovskites [2,4,22,84,85] and metal halides [5,84,86,87], which spans from 0.19 Wm⁻¹K⁻¹ to 0.64 Wm⁻¹K⁻¹ [see Fig. 6(c)]. The complex structure of the halide perovskite Cs₃Bi₂I₆Cl₃ contributes to its ultra-low thermal

conductivity of $0.19 \text{ Wm}^{-1}\text{K}^{-1}$ [85]. Additionally, the chain-axis bond strength of CsCu_2I_3 is similar to the in-plane bond strength of $\text{Cs}_2\text{PbI}_2\text{Cl}_2$ [5]. Consequently, we expect a similar value of $0.37 \text{ Wm}^{-1}\text{K}^{-1}$ for the chain-axis $\kappa_{L,z}$ and lower values for the cross-chain $\kappa_{L,x,y}$, attributable to the weak cross-chain bonding in CsCu_2I_3 . Overall, the predicted total κ_L of CsCu_2I_3 in this study is reasonably reliable and can be verified by future experimental investigations.

IV. CONCLUSIONS

In summary, we have employed a first-principles-based framework that incorporates anharmonic phonon renormalization and a unified theory of thermal transport, accounting for both 3ph and 4ph interaction processes, to investigate the thermal conductivity in CsCu_2I_3 . Our results reveal that the crystalline CsCu_2I_3 , with its unique 1D chain-like structure and characterized by a *cmcm* space group, exhibits unstable soft modes dominated by Cu and I atoms at 0 K. Utilizing the anharmonic phonon renormalization technique, we successfully stabilize the soft modes of CsCu_2I_3 at ~ 75 K. The relatively low phase transition temperature provides an explanation for the experimentally observed CsCu_2I_3 structure, characterized by a *cmcm* space group at room temperature. By employing a unified theory of thermal transport that considers both the coherences and populations' contributions, we predict a room-temperature κ_L of CsCu_2I_3 to be $0.362 \text{ Wm}^{-1}\text{K}^{-1}$ along the chain axis (Z-axis), $0.201 \text{ Wm}^{-1}\text{K}^{-1}$ along the cross-chain direction (Y-axis), and $0.239 \text{ Wm}^{-1}\text{K}^{-1}$ along the cross-chain direction (X-axis). Meanwhile, the contributions from populations dominate the total chain-axis thermal conductivity, while the coherences' contributions start to take the lead in the total cross-chain thermal conductivity above 442 K. The dominance of $\kappa_{L,y}^C$ in the cross-chain thermal conductivity of CsCu_2I_3 can be traced back to its unique chain-like 1D structure. This unique structure, characterized by weak bonding, results in

an exceedingly low cross-chain $\kappa_{L,y}^P$, exceptionally small cross-chain group velocities, and strong 4ph scatterings, all of which collectively facilitate the wave-like tunnelling of phonons. Furthermore, our predictions unveil an unexpected anomalous trend of increasing cross-chain thermal conductivity with increasing temperature across the entire temperature range, which is atypical for a single crystal. We categorize this phenomenon as an abnormal glass-like behavior of thermal conductivity and attribute it to the dominant role of cross-chain coherences' conductivity in thermal transport of CsCu₂I₃. Our study emphasizes that the conventional Peierls-Boltzmann transport equation falls short in elucidating the thermal transport in crystalline CsCu₂I₃. It further suggests that a comprehensive understanding of thermal transport in CsCu₂I₃ can be achieved by considering both 3ph and 4ph scattering effects on phonon energies, the particle-like phonon propagation, and the wave-like tunnelling of phonons. Finally, our work not only offers insights into the nature of lattice thermal transport in 1D metal halides but also suggests a potential new avenue for engineering phonon-related properties.

ACKNOWLEDGEMENT

We are thankful for the financial support from the Science and Technology Planning Project of Guangdong Province, China (Grant No. 2017A050506053), the Science and Technology Program of Guangzhou (No. 201704030107), and the Hong Kong General Research Fund (Grants No. 16214217 and No. 16206020). This paper was supported in part by the Project of Hetao Shenzhen-Hong Kong Science and Technology Innovation Cooperation Zone (HZQB-KCZYB2020083). R.G. acknowledges support from the Excellent Young Scientists Fund (Overseas) of Shandong Province (2022HWYQ091) and the Initiative Research Fund of Shandong Institute of Advanced Technology (2020107R03). C.L. acknowledges the support from the Sinergia project of the Swiss National Science Foundation (grant number CRSII5_189924).

References

- [1] T. Matsunaga, N. Yamada, R. Kojima, S. Shamoto, M. Sato, H. Tanida, T. Uruga, S. Kohara, M. Takata, and P. Zalden, *Advanced Functional Materials* **21**, 2232 (2011).
- [2] H. Xie, S. Hao, J. Bao, T. J. Slade, G. J. Snyder, C. Wolverton, and M. G. Kanatzidis, *J. Am. Chem. Soc.* **142**, 9553 (2020).
- [3] M. A. Green and S. P. Bremner, *Nature materials* **16**, 23 (2017).
- [4] W. Lee, H. Li, A. B. Wong, D. Zhang, M. Lai, Y. Yu, Q. Kong, E. Lin, J. J. Urban, and J. C. Grossman, *Proceedings of the National Academy of Sciences* **114**, 8693 (2017).
- [5] P. Acharyya, T. Ghosh, K. Pal, K. Kundu, K. Singh Rana, J. Pandey, A. Soni, U. V. Waghmare, and K. Biswas, *J. Am. Chem. Soc.* **142**, 15595 (2020).
- [6] T. Sadi, I. Radevici, and J. Oksanen, *Nature Photonics* **14**, 205 (2020).
- [7] L. E. Bell, *Science* **321**, 1457 (2008).
- [8] G. J. Snyder and E. S. Toberer, *Nature materials* **7**, 105 (2008).
- [9] X. Zhou, Y. Yan, X. Lu, H. Zhu, X. Han, G. Chen, and Z. Ren, *Materials Today* **21**, 974 (2018).
- [10] S. Bai, P. Da, C. Li, Z. Wang, Z. Yuan, F. Fu, M. Kawecki, X. Liu, N. Sakai, and J. T. Wang, *Nature* **571**, 245 (2019).
- [11] M. A. Green, A. Ho-Baillie, and H. J. Snaith, *Nature photonics* **8**, 506 (2014).
- [12] C. C. Boyd, R. Checharoen, T. Leijtens, and M. D. McGehee, *Chem. Rev.* **119**, 3418 (2018).

- [13] G. Divitini, S. Cacovich, F. Matteocci, L. Cinà, A. Di Carlo, and C. Ducati, *Nature Energy* **1**, 1 (2016).
- [14] T. Lanigan-Atkins, X. He, M. J. Krogstad, D. M. Pajerowski, D. L. Abernathy, G. N. Xu, Z. Xu, D. Chung, M. G. Kanatzidis, and S. Rosenkranz, *Nature materials* **20**, 977 (2021).
- [15] Y. He and G. Galli, *Chemistry of Materials* **26**, 5394 (2014).
- [16] I. Chung, J. Song, J. Im, J. Androulakis, C. D. Malliakas, H. Li, A. J. Freeman, J. T. Kenney, and M. G. Kanatzidis, *J. Am. Chem. Soc.* **134**, 8579 (2012).
- [17] C. C. Stoumpos, C. D. Malliakas, and M. G. Kanatzidis, *Inorg. Chem.* **52**, 9019 (2013).
- [18] M. A. Haque, S. Kee, D. R. Villalva, W. Ong, and D. Baran, *Advanced Science* **7**, 1903389 (2020).
- [19] J. Klarbring, O. Hellman, I. A. Abrikosov, and S. I. Simak, *Phys. Rev. Lett.* **125**, 045701 (2020).
- [20] J. R. Sootsman, D. Y. Chung, and M. G. Kanatzidis, *Angewandte Chemie International Edition* **48**, 8616 (2009).
- [21] A. Pisoni, J. Jacimovic, O. S. Barisic, M. Spina, R. Gaál, L. Forró, and E. Horváth, *The journal of physical chemistry letters* **5**, 2488 (2014).
- [22] A. Bhui, T. Ghosh, K. Pal, K. Singh Rana, K. Kundu, A. Soni, and K. Biswas, *Chemistry of Materials* **34**, 3301 (2022).
- [23] C. Wu, Q. Zhang, G. Liu, Z. Zhang, D. Wang, B. Qu, Z. Chen, and L. Xiao, *Advanced Energy Materials* **10**, 1902496 (2020).
- [24] P. Gao, A. R. Bin Mohd Yusoff, and M. K. Nazeeruddin, *Nature communications* **9**, 5028 (2018).
- [25] J. Sun and C. A. Ullrich, *Physical Review Materials* **4**, 095402 (2020).

- [26] R. Roccanova, A. Yangui, G. Seo, T. D. Creason, Y. Wu, D. Y. Kim, M. Du, and B. Saparov, *ACS Materials Letters* **1**, 459 (2019).
- [27] P. Cheng, L. Sun, L. Feng, S. Yang, Y. Yang, D. Zheng, Y. Zhao, Y. Sang, R. Zhang, and D. Wei, *Angewandte Chemie* **131**, 16233 (2019).
- [28] T. Jun, K. Sim, S. Iimura, M. Sasase, H. Kamioka, J. Kim, and H. Hosono, *Adv Mater* **30**, 1804547 (2018).
- [29] B. Yang, L. Yin, G. Niu, J. Yuan, K. Xue, Z. Tan, X. Miao, M. Niu, X. Du, and H. Song, *Adv Mater* **31**, 1904711 (2019).
- [30] Q. Li, Z. Chen, B. Yang, L. Tan, B. Xu, J. Han, Y. Zhao, J. Tang, and Z. Quan, *J. Am. Chem. Soc.* **142**, 1786 (2020).
- [31] R. Lin, Q. Guo, Q. Zhu, Y. Zhu, W. Zheng, and F. Huang, *Adv Mater* **31**, 1905079 (2019).
- [32] X. Mo, T. Li, F. Huang, Z. Li, Y. Zhou, T. Lin, Y. Ouyang, X. Tao, and C. Pan, *Nano Energy* **81**, 105570 (2021).
- [33] Z. Xing, Z. Zhou, G. Zhong, C. C. Chan, Y. Li, X. Zou, J. E. Halpert, H. Su, and K. S. Wong, *Advanced Functional Materials* **32**, 2207638 (2022).
- [34] J. Luo, X. Wang, S. Li, J. Liu, Y. Guo, G. Niu, L. Yao, Y. Fu, L. Gao, and Q. Dong, *Nature* **563**, 541 (2018).
- [35] Y. Jung, I. T. Han, Y. C. Kim, and A. Walsh, *npj Computational Materials* **7**, 51 (2021).
- [36] J. W. Park, Y. Jung, and A. Walsh, arXiv preprint arXiv:2305.11745 (2023).
- [37] T. Tadano and W. A. Saidi, *Phys. Rev. Lett.* **129**, 185901 (2022).
- [38] B. Huang, J. Zheng, C. Lin, C. Lin, G. Hautier, and R. Guo, (2023).
- [39] L. Xie, J. H. Feng, R. Li, and J. Q. He, *Phys. Rev. Lett.* **125**, 245901 (2020).

- [40] Y. Xia, V. Ozoliņš, and C. Wolverton, *Phys. Rev. Lett.* **125**, 085901 (2020).
- [41] Y. Xia, K. Pal, J. He, V. Ozoliņš, and C. Wolverton, *Phys. Rev. Lett.* **124**, 065901 (2020).
- [42] G. P. Srivastava, *The physics of phonons* (Routledge, 2019).
- [43] R. Hanus, J. George, M. Wood, A. Bonkowski, Y. Cheng, D. L. Abernathy, M. E. Manley, G. Hautier, G. J. Snyder, and R. P. Hermann, *Materials Today Physics* **18**, 100344 (2021).
- [44] Y. Luo, X. Yang, T. Feng, J. Wang, and X. Ruan, *Nature communications* **11**, 2554 (2020).
- [45] S. Mukhopadhyay, D. S. Parker, B. C. Sales, A. A. Puretzky, M. A. McGuire, and L. Lindsay, *Science* **360**, 1455 (2018).
- [46] M. Simoncelli, N. Marzari, and F. Mauri, *Nature Physics* **15**, 809 (2019).
- [47] M. Simoncelli, N. Marzari, and F. Mauri, *Physical Review X* **12**, 041011 (2022).
- [48] P. E. Blöchl, *Physical review B* **50**, 17953 (1994).
- [49] G. Kresse and J. Furthmüller, *Physical review B* **54**, 11169 (1996).
- [50] J. P. Perdew, A. Ruzsinszky, G. I. Csonka, O. A. Vydrov, G. E. Scuseria, L. A. Constantin, X. Zhou, and K. Burke, *Phys. Rev. Lett.* **100**, 136406 (2008).
- [51] J. P. Perdew, K. Burke, and Y. Wang, *Physical review B* **54**, 16533 (1996).
- [52] S. Hull and P. Berastegui, *Journal of Solid State Chemistry* **177**, 3156 (2004).
- [53] K. Esfarjani and H. T. Stokes, *Physical Review B* **77**, 144112 (2008).
- [54] A. Togo and I. Tanaka, *Scr. Mater.* **108**, 1 (2015).
- [55] F. Zhou, W. Nielson, Y. Xia, and V. Ozoliņš, *Physical Review B* **100**, 184308 (2019).

- [56] E. J. Candès and M. B. Wakin, IEEE Signal Process. Mag. **25**, 21 (2008).
- [57] T. Tadano and S. Tsuneyuki, Physical Review B **92**, 054301 (2015).
- [58] L. J. Nelson, G. L. Hart, F. Zhou, and V. Ozoliņš, Physical Review B **87**, 035125 (2013).
- [59] T. Tadano, Y. Gohda, and S. Tsuneyuki, Journal of Physics: Condensed Matter **26**, 225402 (2014).
- [60] C. Lin, S. Poncé, and N. Marzari, npj Computational Materials **8**, 236 (2022).
- [61] T. Tadano and S. Tsuneyuki, Phys. Rev. Lett. **120**, 105901 (2018).
- [62] I. Errea, B. Rousseau, and A. Bergara, Phys. Rev. Lett. **106**, 165501 (2011).
- [63] J. Zheng, D. Shi, Y. Yang, C. Lin, H. Huang, R. Guo, and B. Huang, Physical Review B **105**, 224303 (2022).
- [64] J. Zheng, D. Shi, S. Liu, Y. Yang, C. Lin, Z. Chang, R. Guo, and B. Huang, Physical Review Materials **6**, 093801 (2022).
- [65] W. Li, J. Carrete, N. A. Katcho, and N. Mingo, Comput. Phys. Commun. **185**, 1747 (2014).
- [66] T. Feng and X. Ruan, Physical Review B **93**, 045202 (2016).
- [67] Z. Han, X. Yang, W. Li, T. Feng, and X. Ruan, Comput. Phys. Commun. **270**, 108179 (2022).
- [68] S. Tamura, Physical Review B **27**, 858 (1983).
- [69] P. B. Allen and J. L. Feldman, Physical Review B **48**, 12581 (1993).
- [70] See the Supplemental Material at xxx for parameters containing harmonic and anharmonic phonon properties and thermal conductivity. (unpublished).
- [71] J. Zheng, *First-Principles Study of Thermal Transport in Highly Anharmonic Materials and Complex Crystalline Polymers* (Hong Kong University of Science and Technology (Hong Kong), 2022).

- [72] J. Zheng, D. Shi, Y. Yang, C. Lin, H. Huang, R. Guo, and B. Huang, *Physical Review B* **105**, 224303 (2022).
- [73] T. Tadano, Y. Gohda, and S. Tsuneyuki, *Phys. Rev. Lett.* **114**, 095501 (2015).
- [74] W. Li and N. Mingo, *Physical Review B* **91**, 144304 (2015).
- [75] J. M. Skelton, L. A. Burton, S. C. Parker, A. Walsh, C. Kim, A. Soon, J. Buckeridge, A. A. Sokol, C. R. A. Catlow, and A. Togo, *Phys. Rev. Lett.* **117**, 075502 (2016).
- [76] E. L. Da Silva, J. M. Skelton, S. C. Parker, and A. Walsh, *Physical Review B* **91**, 144107 (2015).
- [77] L. Huang and W. R. Lambrecht, *Physical Review B* **90**, 195201 (2014).
- [78] J. He, Y. Xia, W. Lin, K. Pal, Y. Zhu, M. G. Kanatzidis, and C. Wolverton, *Advanced Functional Materials* **32**, 2108532 (2022).
- [79] T. M. Tritt, *Thermal conductivity: theory, properties, and applications* (Springer Science & Business Media, 2005).
- [80] W. Li and N. Mingo, *Physical Review B* **91**, 144304 (2015).
- [81] Z. Zeng, C. Zhang, N. Ouyang, and Y. Chen, *Physical Review B* **106**, 054302 (2022).
- [82] A. F. Ioffe and A. R. Regel, *FA Kroger, and RE Burgess* (Heywood, London, 1960) **4**, 237 (1960).
- [83] P. Cheng, N. Shulumba, and A. J. Minnich, *Physical Review B* **100**, 094306 (2019).
- [84] T. Haeger, M. Ketterer, J. Bahr, N. Pourdavoud, M. Runkel, R. Heiderhoff, and T. Riedl, *Journal of Physics: Materials* **3**, 024004 (2020).
- [85] P. Acharyya, T. Ghosh, K. Pal, K. S. Rana, M. Dutta, D. Swain, M. Etter, A. Soni, U. V. Waghmare, and K. Biswas, *Nature communications* **13**, 5053 (2022).
- [86] T. Haeger, M. Wilmes, R. Heiderhoff, and T. Riedl, *The Journal of Physical Chemistry Letters* **10**, 3019 (2019).

[87] Z. Zeng, C. Chen, C. Zhang, Q. Zhang, and Y. Chen, *Physical Review B* **105**, 184303 (2022).

[88] L. Lindsay, C. Hua, X. L. Ruan, and S. Lee, *Materials Today Physics* **7**, 106 (2018).